OPEN ACCESS

ARTICLE

The Innovation Geoscience

Floating iron biofilms as hidden barriers to methane emissions in wetlands

Sha Zhang,[1,2,3] Qianrui Huangfu,[3] Dong Zhu,[1,2] and Zheng Chen[3,*]

*Correspondence: Zheng.Chen@xjtlu.edu.cn

Received: March 23, 2025; Accepted: July 16, 2025; Published Online: July 29, 2025; https://doi.org/10.59717/j.xinn-geo.2025.100161

GRAPHICAL ABSTRACT

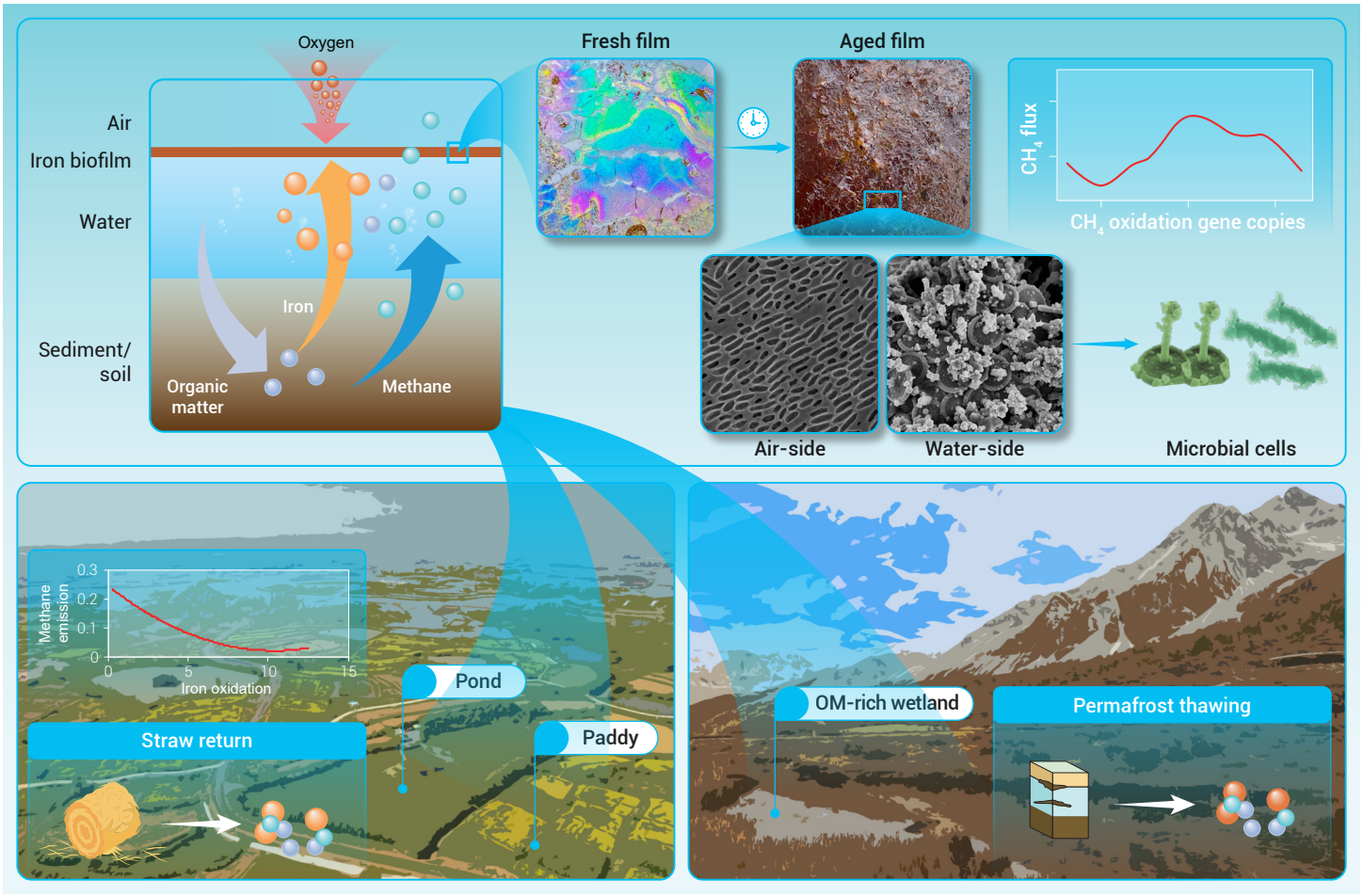

PUBLIC SUMMARY

- Iron biofilms, iridescent or rust-stained, are widely observed in shallow water systems.
- Iron biofilms at wetland water-air interfaces can reduce methane emissions by up to 6.9-fold.
- We challenge the long-held idea that methane oxidation occurs mainly at the sediment-water interface.
- Iron biofilms are long-lasting, sustaining their methane-barrier function over time
- This process offers a nature-based solution for controlling methane emissions in wetlands.

ARTICLE

OPEN ACCESS

Floating iron biofilms as hidden barriers to methane emissions in wetlands

Sha Zhang,[1,2,3] Qianrui Huangfu,[3] Dong Zhu,[1,2] and Zheng Chen[3,*]

[1]State Key Laboratory of Regional and Urban Ecology, Ningbo Observation and Research Station, Institute of Urban Environment, Chinese Academy of Sciences, Xiamen 361021, China
[2]Zhejiang Key Laboratory of Pollution Control for Port-Petrochemical Industry, CAS Haixi Industrial Technology Innovation Center in Beilun, Ningbo 315830, China
[3]Department of Health and Environmental Sciences, Xi'an Jiaotong-Liverpool University, 111 Ren'ai Road, Suzhou 215123, China
*Correspondence: Zheng.Chen@xjtlu.edu.cn

Received: March 23, 2025; Accepted: July 16, 2025; Published Online: July 29, 2025; https://doi.org/10.59717/j.xinn-geo.2025.100161

Citation: Zhang S., Huangfu Q., Zhu D., et al. (2025). Floating iron biofilms as hidden barriers to methane emissions in wetlands. *The Innovation Geoscience* **3**:100161.

Wetland methane emissions are primarily mitigated by microbial oxidation at the sediment-water interface (SWI). Yet, this paradigm fails to explain persistent methane oversaturation in surface waters and lower-than-expected emissions. Here, we demonstrate an overlooked methane barrier formed at water–air interfaces (WAI) by self-organized iron biofilms. Organic matter inputs destabilize the SWI, enabling ferrous iron to diffuse upward and become oxidized, resulting in the formation of iron biofilms ranging in thicknesses from nanometers to centimeters at the WAI. This iron film barrier reduces methane emissions by 2.4- to 6.9-fold through physical entrapment and microbial oxidation (e.g., *pmoA* gene abundance: 2.1×10^8 copies m^{-2}), involving communities dominated by aerobic and facultative heterotrophs, as well as nitrate- and sulfur-respiring taxa. The dual methane-barrier paradigm explains emission paradoxes in straw-amended environments. This mechanism, absent from the Intergovernmental Panel on Climate Change models, could revise global methane budget estimates and guide nature-based solutions to mitigate wetland methane emissions.

INTRODUCTION

Wetlands are unique ecosystems characterized by frequent or continuous flooding, or near-surface water saturation.[1] Wetlands contribute 30–40% of global methane, a potent greenhouse gas for global warming.[2] For rice fields alone, there is about 29 Tg yr^{-1} emission budget.[2] Despite their climate significance, wetland methane fluxes remain poorly constrained in statistical models,[1,3,4] largely due to unresolved methane consumption and exchange processes at two critical interfaces: the sediment/soil-water interface (SWI) and the water-air interface (WAI).[4-10]

Microbes at the SWI can oxidize 40–100% of methane,[1,3,9-13] thereby forming a natural methane 'barrier'. This activity is driven by respiratory processes that use oxygen,[14] nitrate[15], iron,[13,16-19] and sulfate[15,20] as terminal electron acceptors. However, the SWI methane-barrier can collapse under high organic matter (OM) conditions, such as eutrophic lakes[21,22] or rice paddies with straw incorporation,[23] allowing methane to leak into surface waters.[15,19] Paradoxically, these methane-rich lake waters often emit far less methane than predicted,[8,24-26] and emissions from straw-amended rice fields also plateau beyond ~6.4 tons ha^{-1}.[27] These discrepancies suggest unrecognized methane sinks at critical interfaces.

Iron biogeochemistry may resolve this paradox, especially in freshwater environments.[13,17,18,28] While iron-mediated methane oxidation is well-studied at the SWI,[20,22] high OM inputs redistribute the redox interface to the WAI,[29] where ferrous ions oxidize into films or flocs.[30-33] These films, commonly observed in shallow wetlands,[30,34-36] could act as secondary methane-barriers. Yet, no studies have quantified their methane-barrier capacity or identified the microbial communities responsible for this process, despite their widespread occurrence and ecological importance.

In this study, we challenge the SWI methane-barrier paradigm by proposing a dual methane-barrier hypothesis: iron films at the WAI compensate for SWI failure in high-OM wetlands. Using a novel protocol to generate iron films from soils/sediments, we integrate methane flux/solubility measurements, geochemical analyses, and microbial genomics to test the proposed dual methane-barrier paradigm.

MATERIALS AND METHODS

Sediments and soils

A total of 30 sediment and paddy soil samples were collected from different regions of China, including one lake sediment, one coastal sediment, and 28 paddy samples (Figure 1A). The samples were wet sieved through a 2-mm mesh to remove debris, then stored in sealed plastic containers submerged under a 5–15 cm water column. Each container contained at least 10 kg of soil/sediment sample. During preservation, 0.2 g sediment/soil paste was sampled, dried and extracted by 6 M hydrochloric acid (HCl) for iron content analysis by inductively coupled plasma mass spectrometry (ICP–MS, Perkins 350A). Soil paste pH was measured directly using a glass pH electrode. Soil OM was measured by loss-on-ignition. Initial iron content ranged from 0.1 g kg^{-1} in coastal sediment to 88 g kg^{-1} in paddy soil, with an average of 21.5 ± 16.1 g kg^{-1}. Soil OM content averaged 2.4 ± 0.6%, ranging from 0.9% to 3.9%, while pH values varied between 5.5 and 7.9 (mean: 6.5 ± 0.6). More details on soil properties are included in Table S1.

Experimental design

A series of distinctive experiments were conducted in diverse sedimentary environments. The experimental design is summarized in Figure S1. Unless otherwise specified, all experiments were conducted in custom-made PVC (polyvinyl chloride) pots (10 cm × 10 cm × 15 cm) under flooded conditions with a 5 cm water layer at 25 °C. Methane fluxes were measured using chamber-based methods, and samples (e.g., floating iron films, water, and surface sediments/soils) were collected for DNA extraction, *pmoA* gene quantification, and chemical characterization. Key aspects of the experiments are described in later sections.

Chamber-based methane flux measurement

Methane fluxes were measured using a chamber-based method with a LI-COR methane analyzer (LI-7810, LI-COR Biosciences) used for determining the slope of methane concentrations.[37] Methane flux was calculated based on the initial rate of change i.e., slope in methane concentration (∂C/∂t) using the following equation:

$$J_{CH_4} = \frac{\partial C_{CH_4}}{\partial t} \times \frac{V}{A} \times \frac{P(1-W_0)}{RT},$$

where J_{CH_4} is methane flux expressed as μmol m^{-2} s^{-1}. V is the chamber volume (0.002550 m^3), P is the atmospheric pressure (101.3 kPa), W_0 is the initial water vapor mole fraction, R is the gas constant (0.008134 m^3 kPa mol^{-1} K^{-1}), A is the soil area (0.0007065 m^2), T is the soil temperature (K) at a 5cm depth, $\frac{\partial C_{CH_4}}{\partial t}$ is the mole fraction of methane in μmol mol^{-1} over time (s).

Methane dissolution

Dissolved methane concentrations in water or gaseous methane in bubbles were measured using a headspace equilibration technique.[38] In this method, water samples were placed in sealed vials, allowing methane in the water to equilibrate with a nitrogen headspace above the water. The samples were equilibrated for 30 minutes at 25°C. The methane concentration in the headspace was then quantified using Agilent 7890B GC equipped with a flame ionization detector. Calibration was performed using certified methane standards (0–40.7 μmol L^{-1}).

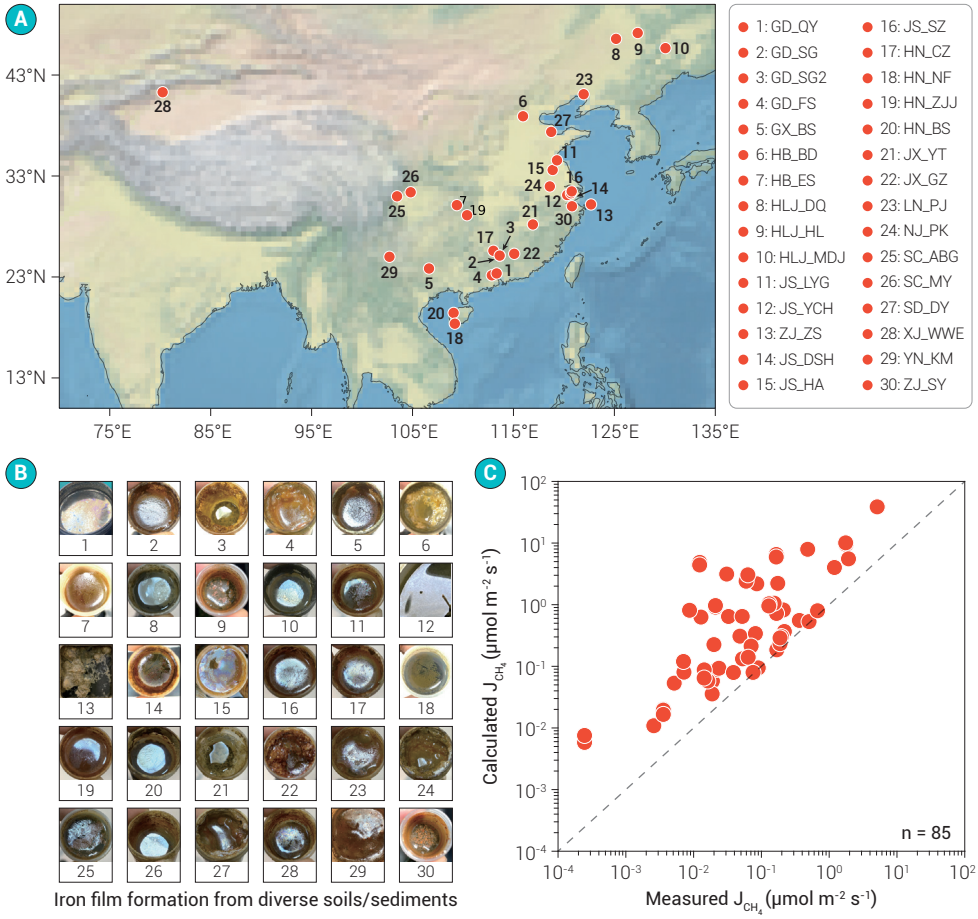

Figure 1. Iron film formation and their methane-barrier effect across diverse soils and sediments in China (A) Map of the 30 soils and sediments used for iron film cultivation. (B) Representative images showing the formation and structural features of iridescent iron films. (C) Comparison of measured diffusive methane fluxes above the water surface and those calculated using Fick's law (dashed line indicates 1:1 ratio).

Diffusive methane flux calculation

Diffusive methane flux was calculated using Fick's law[38] as follows:

$$J_{CH_4} = K(C_w - C_a),$$

where J_{CH_4} is the measured methane flux in μmol m^{-2} s^{-1}, K is the mass-transfer coefficient (1.7 cm h^{-1} at zero-to-low wind speed condition[38]), C_w is the measured concentration of dissolved methane in the water (mol m^{-3}), C_a is the calculated concentration of methane in equilibrium with the atmospheric gas concentration. C_a is calculated as:

$$C_a = P_p\beta,$$

where P_p was the measured atmospheric concentration of CH_4 (atm). β is the Bunsen solubility coefficient mL (L atm)$^{-1}$. At 1 atm and 24°C, β = 0.03211 mL L^{-1} atm^{-1}.

In-situ methane flux measurement

In-situ methane concentrations were measured using the LI-COR gas analyzer. To expose areas without iron films, a small drop of water was applied to disrupt the iron film on the sediment surface, creating exposed patches. After allowing 5–10 min for stabilization, the gas analyzer intake was positioned in an ambient environment to measure the background methane levels. The intake was then placed 2 mm above the exposed patch, with the exhaust positioned downstream to minimize interference with methane emissions. Continuous measurements were recorded for at least 30 s, followed by a second background methane concentration reading after moving the intake back to the ambient environment. This process was repeated 2–3 times at randomly selected locations near the disrupted iron film.

Iridescent iron films formation and methane-barrier function

We assume that OM inputs drive the formation of iridescent iron film in fields. To test this hypothesis, sediment and soil samples (n = 30) were homogenized and incubated under flooded conditions at 25°C. To stimulate microbial activity, glucose (0.5% wet weight) was added into 50 mL falcon tubes. Iridescent or rusty-colored iron films developed within several days and weeks. Methane fluxes and dissolved methane concentrations beneath the films were measured over time. For methane flux measurements during early bubble formation, where large bubbles accumulated on the water surface, but no visible iron films were present, these measurements were excluded from the final analysis. This absence of films reflects initial microbial fermentation, which rapidly produces volatile organic compounds and precedes iron reduction and methanogenesis.

Effect of continuous iron film removal

While comparing methane fluxes with and without iron films at a single time point is straightforward, such comparisons cannot capture the cumulative barrier effect throughout an entire OM-stimulated methane emission peak. To address this limitation, we conducted a short-term (14-day) experiment using paddy soil from the ZJ_SY site, China (Figure 1A), to examine the impact of continuous iron film removal on methane emissions. The soil was passed through a 2-mm sieve, homogenized manually, and adjusted to ~35% moisture content. Air-dried old rice straw (equivalent to 8 t ha^{-1}) was crushed by blenders and mixed with 300 g of moist soil. Daily iron film removal began on Day 3, and methane fluxes were measured daily throughout the experiment. In addition, due to the reduced yield of iron films caused by daily removal, samples from different pots were pooled into a single composite sample for DNA extraction.

Temporal methane-barrier dynamics

In contrast, a longer-term (49-day) experiment using lake sediment from the JS_DSH site (China, Figure 1A) was designed to investigate the durability and temporal evolution of the methane-barrier function of intact iron films under limited disturbance. Here, iron films were left largely undisturbed, except for deliberate disruptions on Day 7 (partial) and Day 49 (complete), to assess barrier persistence and functional recovery. Methane flux measurements started 1.5 hours after glucose amendment, with high-frequency sampling during the first 5 days. Water samples (0.5 mL) were collected beneath iron films on Days 3 and 49 for determining methane dissolutions. On Day 7, *in-situ* methane flux were measured above both intact iron films and adjacent disturbed areas (~2 mm diameter) by water droplet to show real-time flux differences between these conditions. Methane bubbles formed at the WAI were sampled on Day 49 using a gas-tight syringe (0.5 mL per sample) for gas concentration analysis.

Methane emission in response to fresh straw incorporation

A 7-day incubation examined the methane-barrier effect under fresh rice straw incorporation in three paddy soils (GD_QY, HB_ES, JS_YCH) and one coastal sediment (ZJ_ZS, Figure 1A). Fresh rice straw (8 t ha^{-1}) was cut into 0.5 cm strips and incorporated into 600 g of air-dried soil or 0.001 m^3 sediment sludge in four replicates per soil type. Methane fluxes were measured daily, and comparative flux measurements were conducted with and without

floating iron films. Samples were collected for microbial and geochemical analyses. These samples were taken from each pot for all four replicates, resulting in a total of 16 samples per sample type (film, water, and sediment/soil) across the experiment.

Greenhouse study with postharvest straw incorporation

To investigate whether methane emissions under varying straw incorporation rates are associated with the production of iron films, we conducted a greenhouse experiment using the JS_YCH paddy soil. Following rice harvest, 5 cm of stubble was retained, and straw was returned directly to each pot to simulate typical field straw-returning practices. Postharvest straw incorporation rates were set at 0, 2, 4, 8 and 12 t ha^{-1}, representing scenarios of no straw return (0 t ha^{-1}), partial returning (2 and 4 t ha^{-1}), full returning (8 t ha^{-1}; all straw returned to the pot from which it was harvested), and excess returning (12 t ha^{-1}). Continuous flooding was maintained with around 5cm water depth throughout the experiment, and methane fluxes were measured daily. In addition to floating iron films, abundant iron flocs were observed in the overlying water. On Day 7, iron film, water, and surface soil samples from the 8 t ha^{-1} treatment were collected for microbial analysis, with two replicates per sample type.

Soil DNA extraction, qPCR and sequencing

Floating iron films (0.4-0.5 g wet weight), water beneath films (5 mL) and surface soil samples (~0.5 g wet weight) were collected from three environments: rice paddies, lakes, and coastal systems. Samples were collected using glass coverslips (22 mm × 22 mm) or 5 mL syringes. Total DNA was extracted using the DNeasy PowerSoil Kit (QIAGEN) following the manufacturer's protocols. Bacterial 16S rRNA (V4 region) was amplified by qPCR using the primer set 515F/806R. Sequencing was performed on the Illumina Nextseq2000 platform (Majorbio, Shanghai, China) using a paired-end 2 × 300 bp configuration.

Amplification of *pmoA* gene

The particulate CH_4 monooxygenase gene (*pmoA*) was amplified using primers A189F (5'-GGNGACTGGGACTTCTGG-3') and mb661r (5'- CCGGMGCAACGTCYTTACC-3'). The *pmoA* gene copy number was quantified by qPCR on the Light Cycler 480 II (Roche, Switzerland). Reaction mixtures were prepared with SYBR Green Master Mix (Thermo Fisher), primers, and template DNA in total volume of 20 μL. Thermal cycling conditions included an initial denaturation step at 94°C for 2 minutes, followed by 42 cycles of denaturation at 94°C for 45 seconds, annealing at 53°C for 45 seconds, and extension at 72°C for 45 seconds. A melt curve analysis was performed to confirm amplification specificity. Quantification was based on standard curves generated from serial dilutions of a cloned *pmoA* amplicon.

Microbial community analysis

Raw sequences were processed using QIIME 1.9.1 and the Uparse pipeline (v7.0.1090). Non-redundant sequences were extracted, chimeras removed, and OTUs clustered at 97% similarity. Representative sequences were classified taxonomically using the RDP Classifier (Release 11.5) at 70% confidence threshold, aligned against the SILVA database (Release 138). Sequences were mapped to representatives at ≥97% similarity to construct the OTU table, and chloroplast sequences were manually removed. To ensure uniform sampling depth for downstream analysis, all samples were rarefied to 50,000 sequences using random subsampling. For taxonomic profiling, sequencing data were processed for taxonomic annotation and analyzed for functional potential using the Functional Annotation of Prokaryotic Taxa (FAPROTAX, v. 1.2.1) database. In addition, alpha diversity metrics (e.g., Shannon and Chao1 index) were calculated to assess within-sample community differences.

Chemical and XRD, SEM, XPS, and fluorescence microscope characterization

In prior iron biofilm sampling for DNA extractions, floating iron films were collected from the water surface using glass slides to preserve the integrity of film structure. Approximately 0.2 g (wet weight) of iron films were collected, freeze-dried, and weighed. Dried samples were dissolved in 0.43 M nitric acid with ultrasonic agitation for 30 minutes. The solution was filtered through a 0.22 μm membrane to remove particulates and diluted 1000-fold. Iron concentrations were quantified using inductively coupled plasma mass spectrometry (ICP-MS, PerkinElmer Model 350).

Replicated slide samples were subjected to XRD analysis on a Bruker D8 Advance diffractometer with Cu Kα radiation (λ = 1.5406 Å). Diffraction patterns were recorded from 5° to 80° 2θ at a step size of 0.02° and a dwell time of 1 second per step, with phases identified using the ICDD database. For morphological analysis, the dried films were coated with a 10-nm gold layer and imaged with a JEOL JSM-7610F SEM at 5 kV. Surface chemistry was examined by X-ray photoelectron spectroscopy (XPS) using a Thermo Scientific K-Alpha system with an Al Kα source, focusing on high-resolution spectra for Fe2p, O1s, and C1s regions. Binding energies were calibrated using the C1s peak at 284.8 eV. Optical microscopy imaging was performed using a Keyence BZ-X810 microscope for bright-field and dark-field fluorescence imaging. Fluorescence excitation utilized LED light sources at 405 nm, 488 nm, and 561 nm. All images were acquired via Z-sectioning at auto-adjusted intervals. Image stacks and merged fluorescence signals were processed using the BZ-X800 Image Converter software.

Statistical analysis

Downstream statistical analysis and data visualization were performed using Python 3.10. Data were visualized using the matplotlib (3.7.1) and seaborn (0.12.2) packages, while statistical analyses were conducted using scipy (1.10.1). Geographical maps were generated using the Cartopy (0.21.1) library. Microbial functional predictions were performed using the FAPROTAX (1.2.1) package. To compare methane fluxes, *pmoA* gene expression levels, and microbial diversity indices between groups, Welch's t-test was employed for pairwise comparisons to account for unequal variances. ANOVA followed by post-hoc Tukey's HSD tests were used for multiple comparisons when data met normality and homoscedasticity assumptions. Statistical significance was determined at $p < 0.05$ for all tests. Non-linear relationships between methane fluxes (JCH_4) and *pmoA* gene abundance were modeled using a Generalized Additive Model (GAM) with a penalized spline term (via the pyGAM package, version 0.8.0). The GAM framework allows flexible, data-driven fitting of non-linear trends without assuming a predefined functional form. A univariate GAM with a cubic spline basis ($s(0)$) was fitted to capture the relationship between log10-transformed *pmoA* gene abundance and log10-transformed methane fluxes. Model predictions were visualized alongside raw data to illustrate trends. A parabolic fit was also applied in selected visualizations to highlight curvature in the correlation. All data points were included in statistical analyses and visualizations.

RESULTS

Organic matter (OM) drives the formation of floating iron film

We demonstrated that OM mediates the formation of iridescent iron films across diverse sediments and soils (Figures 1A–B). Floating iron films were generated by adding 0.5% glucose to flooded soils or sediments, stimulating iron reduction and upward diffusion under controlled conditions. Despite wide geochemical variability among samples (iron: 0.1–88 g kg^{-1}; OM: 0.9–3.9%; pH: 5.5–7.9), iridescent films exhibiting structural color consistently formed within 3–14 days, consistent with prior findings that identifying fresh OM input and flooding as critical drivers.[30] However, without new stimulation, floating iron films continued thickening (Figures S2–S3) but eventually decayed and settled onto the sediment surface within months.

After removing initial surface debris, we recovered smooth, mirror-like films that retained their metallic luster after air- or freeze-drying (Figure S3). This novel coverslip-sampling technique, previously unreported,[30] enabled systematic characterization of film properties. Elemental analysis showed that the films contained ~40% iron, while the overlying water held 4.2 mg L^{-1} of dissolved iron, consistent with iron-carbon dominance reported in previous observations.[34,35]

Model–measurement discrepancies in methane fluxes

The methane-barrier effect is widely supported by discrepancies between calculated and measured methane fluxes in 21 diverse sediment and soil incubations across China. Diffusive methane fluxes calculated using Fick's law and dissolved methane concentrations, were much higher (mean = 1.7,

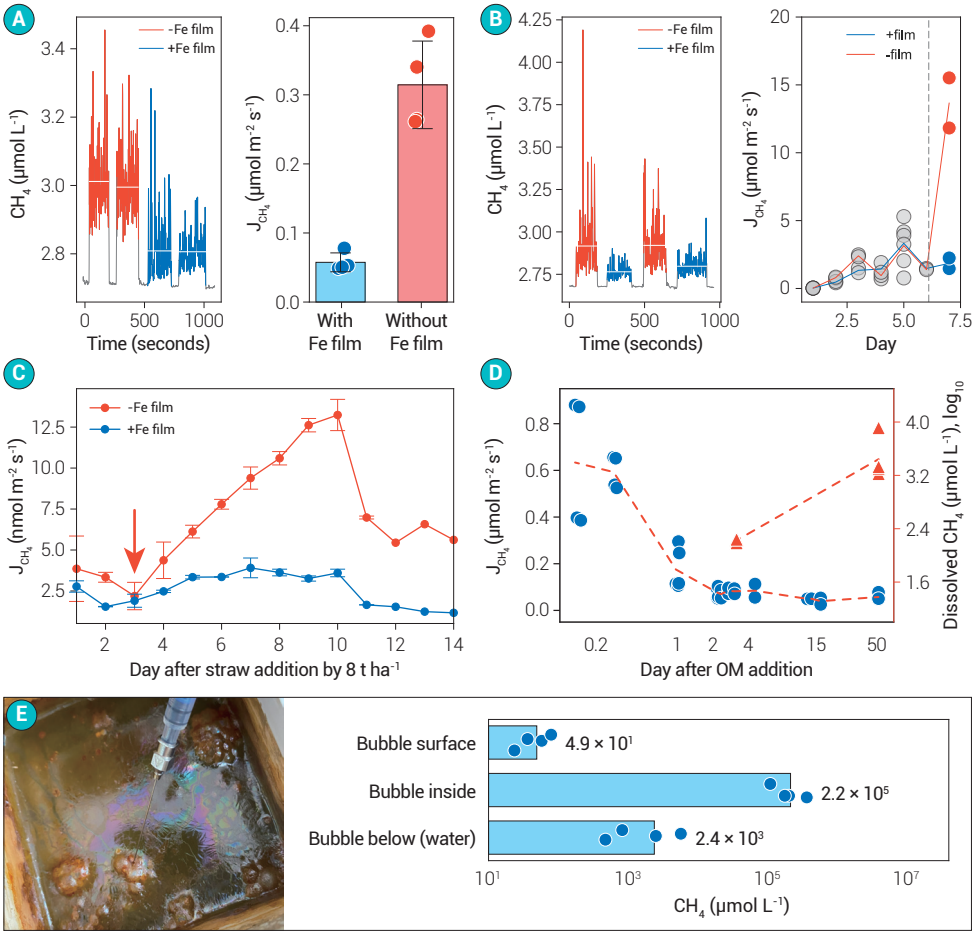

Figure 2. Methane barrier effect of floating iron biofilms across diverse environments (A, B) *In-situ* methane concentrations and fluxes in lake sediment (A; JS_DSH site, Suzhou, China) and coastal sediment (B; ZJ_ZS site, Zhoushan, China). Blue and red lines denote real-time methane concentration dynamics above intact iron films and exposed patches. Right panels: chamber-based flux measurements before and after manual removal of iron films. Dashed vertical line in (B) marks the day of film removal. (C) Methane fluxes in paddy soil (ZJ_SY site, Shangyu, China), comparing treatments with and without daily film removal. (D) Temporal methane flux dynamics and dissolved methane concentrations (Day 3 and 49) in lake sediment amended with OM and incubated for 49 days. Iron biofilms formed naturally during incubation. (E) Methane trapping by aged iron biofilm. Gas was sampled from bubbles trapped beneath iron films, and methane concentrations were measured below, within, and just above the bubble layer at the WAI.

range: 0.0058–39 μmol m^{-2} s^{-1}, n = 85) than the actual measured fluxes (mean = 0.61, range: -0.0039–11 μmol m^{-2} s^{-1}) (Figure 1C). Similar discrepancies have been observed in Florida swamps,[38] where insoluble organic surface films likely suppress gas exchange.[38-40]

Methane barrier effect

The methane-barrier role of floating iron films was experimentally validated by comparing methane fluxes in the presence and absence of the films. For *in-situ* measurements, iron films were locally disturbed using a water droplet, while for chamber-based measurements, the films were completely removed. As shown in Figures 2A-B, diffusive methane fluxes above exposed patches were significantly higher, with fluxes averaging 2.4 times those observed with intact films from lake and coastal sediments. When iron films were manually removed, methane fluxes increased by 4.5-fold in lake sediments, 6.9-fold in coastal sediments, and 2.6-fold in paddy soils (Figures 2A-C). Additionally, continuous removal of the films over a 7-day period caused a sharp increase in methane fluxes from 2 to 13 μmol m^{-2} s^{-1}, further confirming their barrier function (Figure 2C).

Effect duration

Iron films are durable with long-lasting methane-barrier capacity. As shown in Figure 2D, methane fluxes declined sharply from 0.88 to 0.11 μmol m^{-2} s^{-1} and remained low over 49 days. Meanwhile, dissolved methane concentrations beneath the films remained highly supersaturated (up to 3.01×10^8%, far exceeding typical surface water level of 0.01–10 μmol L^{-1} in freshwater marshes). During this period, iron film thickened and physically trapped gas bubbles for weeks (Figure 2E). Methane concentrations within these bubbles reached 21.9% (v/v, n = 4), while dissolved methane in the underlying water ranged1.7–8.2 mmol L^{-1}. In contrast, the methane concentration just 2 mm above the bubble surface was only 49.3 μmol L^{-1} (n = 4), suggesting a steep methane gradient across the iron-rich bubble film that effectively constrained methane exchanges.

Nonlinear microbial regulation of methane fluxes

The methane-barrier effect is supported by methanotrophic communities selectively enriched in iron films across diverse environments (Figure 3). The *pmoA* gene, encoding methane monooxygenase enzyme, was amplificated from iron film, overlying water, and sediment/soil samples. Notably, *pmoA* amplification in water was only detected in samples containing abundant iron flocs (JS_YCH soil, Figures 3A–D).

Specifically, the *pmoA* gene copy numbers in iron films reached 2.1×10^8 copies m^{-2}, slightly lower than those in the surface sediment (p = 0.016, Figure 3B). This supports the dual-barrier hypothesis. In lake sediments, methane fluxes were negatively correlated with *pmoA* gene copies (R^2 = 0.69, p = 0.0009, n = 12, Figure 3C).

Across more diverse environments including costal sediments and four paddy soils, GAM revealed a nonlinear relationship between instant methane flux and *pmoA* gene copies (Figures 3D–E). Specifically, a positive correlation was observed at low methane flux, followed by a negative trend at higher pmoA gene copy numbers. This nonlinear relationship reflects ecological feedback, wherein methane stimulates methanotroph activity, which in turn enhances methane consumption and reduces emissions.

Besides the *pmoA* evidence, the dominance of *Methylophilus* (30.3% relative abundance in paddy films at the ZJ_SY site; Figure 4) supports active methylotrophy involved in methane oxidation. Although microbial composition was assessed via16S rRNA sequencing, the community profiles largely reflect an enrichment effect (e.g., methane-rich water such as that shown in Figure 2E), rather than bulk sediment microbial structure. Co-occurrence network analysis revealed a strong segregation of microbial communities between floating iron biofilms and underlaying sediment at the genus level (Figures S4–5) with minimal taxonomic overlap across different environments. These results suggest that microbial succession at ecotones (e.g., iron film-sediment interfaces) follows a habitat-specific assembly model, driven by localized niche differentiation. For instance, lake iron biofilm harbored unique taxa dominated by *Bacillus*, *Clostridium*, and *Azotobacter*, accounting for 83.1% of identified clones (Figure 4). Among these taxa, a rare yet fast-growing heterotrophic gammaproteobacterium have also been reported as the predominant communities in freshwater surface microlayers.[31,41,42]

Despite ecological filtering at the WAI (Shannon diversity decreased by 62.5%, Chao1 by 45.1% vs. SWI), functional profiling revealed conserved metabolic networks associated with methane oxidation, including sulfur respiration, methanol oxidation, and nitrate reduction (Figure S5). This streamlined diversity, captured through controlled film aging, highlights iron biofilms as simplified yet ecologically representative models for WAI methane cycling.

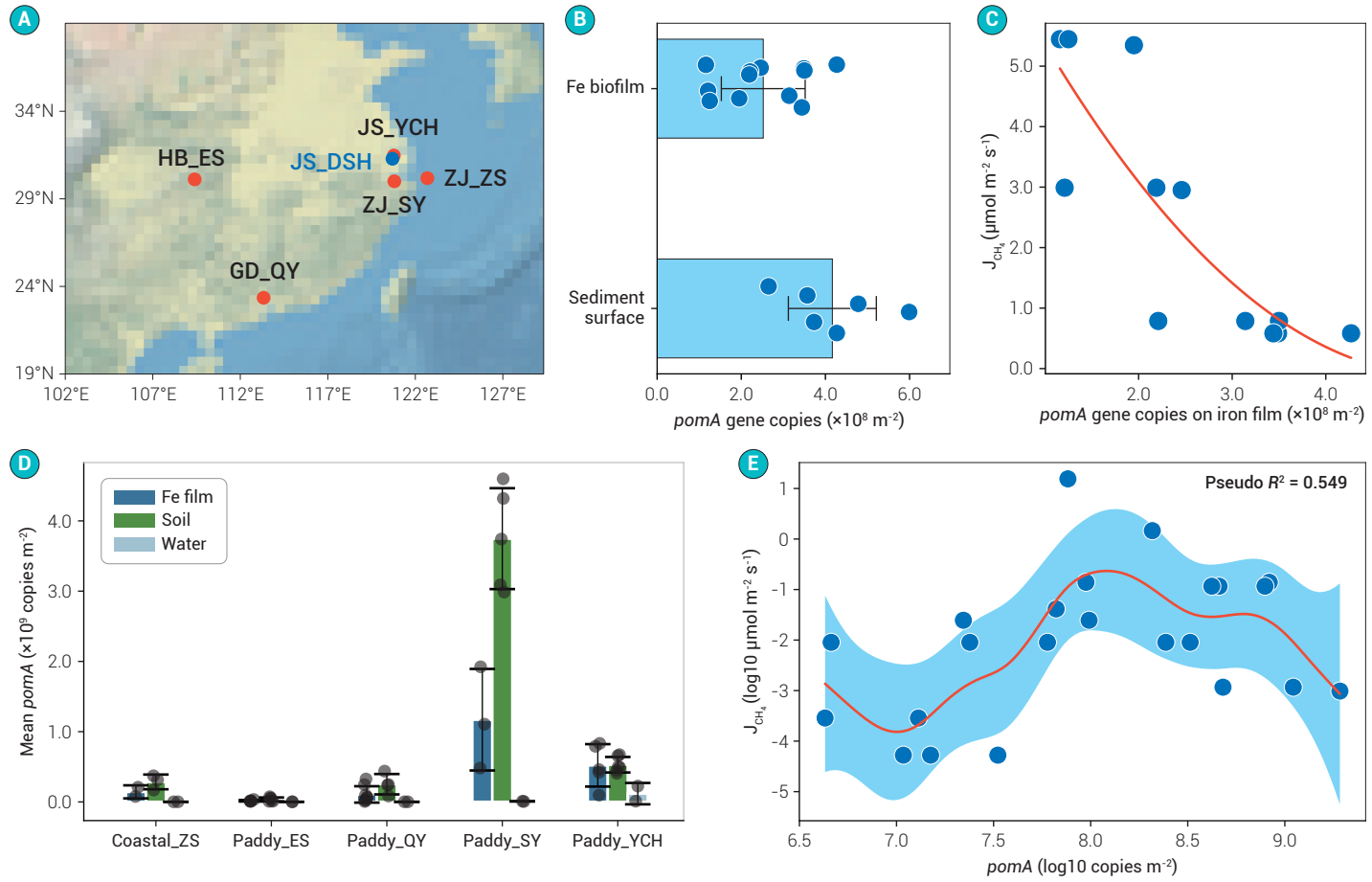

Figure 3. Methanotrophic functional genes across environments (A) Locations of sediment and soil samples used for microbial function analysis. (B) The *pmoA* gene copy numbers in iron biofilms and surface sediment (glucose-amended) from JS_DSH lake. (C) Relationship between methane flux and *pmoA* gene copy number in iron films from JS_DSH lake sediment. (D) The copy number of pmoA gene in films, surface sediments/soils (amended by fresh rice straw) and overlying water in diverse environments. (E) Relationship between methane flux and *pmoA* gene copy number in iron films shown in panel D.

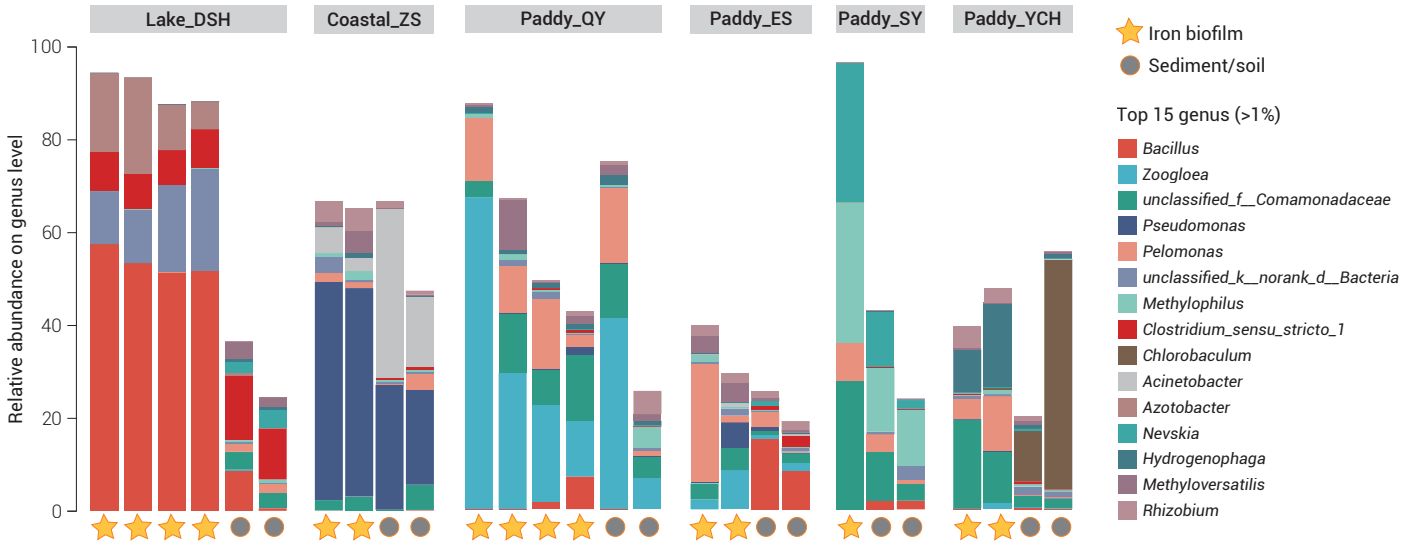

Figure 4. Microbial community composition of iron biofilms and corresponding surface sediments or soils, based on 16S rRNA gene sequencing Only the top 15 bacterial genera with relative abundances greater than 1% are shown. Stars and circles denote microbial communities from iron biofilm and surface sediment/soil samples, respectively.

Unique dual-layer biofilm structure constrains methane exchange

The methane-trapping function of iron films and associated bubbles (Figure 2E) is closely linked to their unique structure and composition (Figures 5 & S6). Scanning electron microscopy observations revealed that fresh films were densely smooth (similar observations in ref[43]), with initial thickness of several hundred nanometers, increasing to several micrometers over time (Figure 5C).

Structurally, the films exhibited a dual-layered architecture: the air-facing surface consisted of tightly packed, self-assembled spherical nanoparticles, while the water-facing side displayed microscale irregularities and biological colonization (Figures 5C-F & S6). Microbial cells were densely arrayed on the water-facing side, particularly on aged films, where rod-shaped and disc-like bacterial aggregates were abundant (Figures 5E–F). This dual-layer mineral-microbial biofilm was consistently observed across diverse environments.

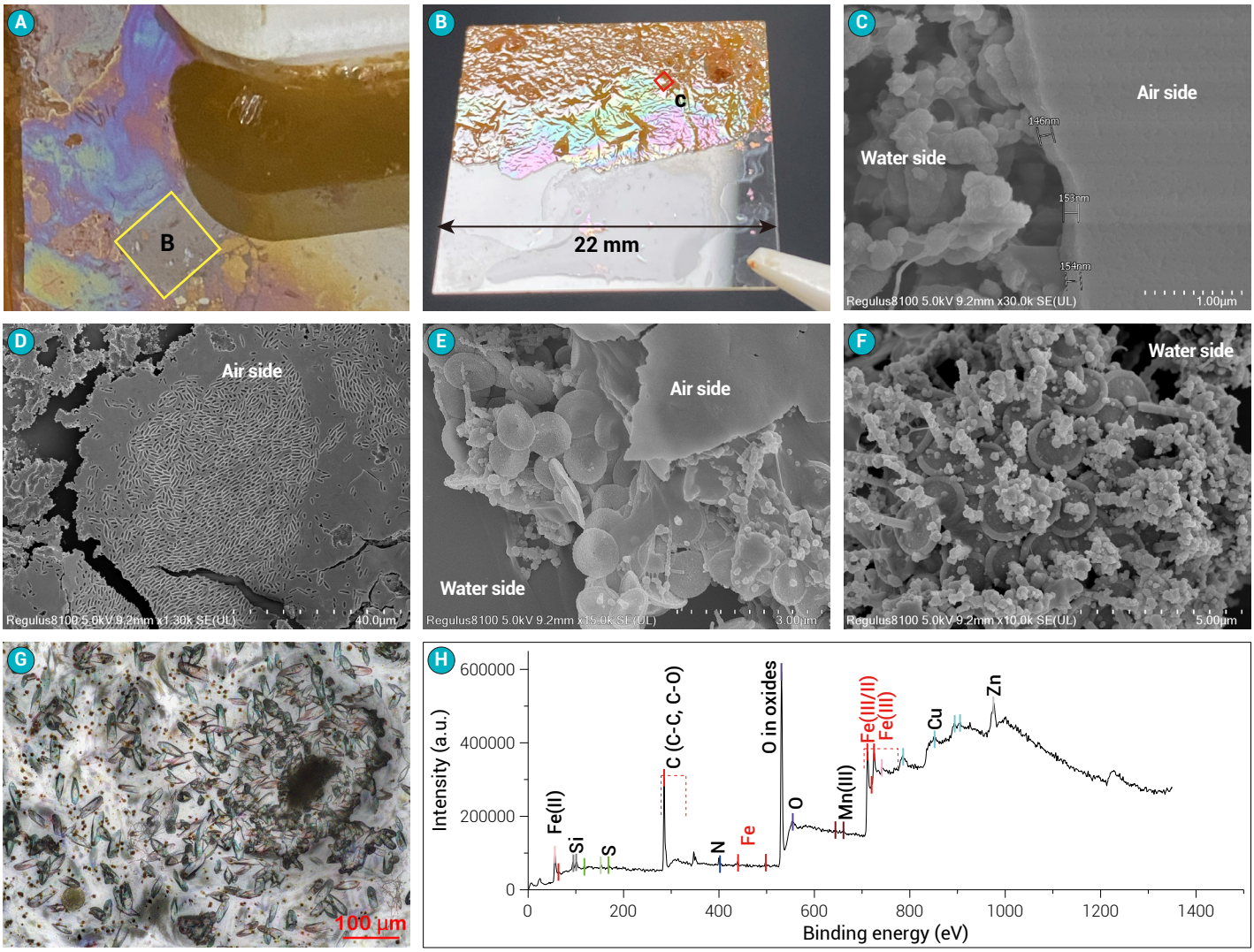

Figure 5. Physical, chemical, and microbial characteristics of floating iron biofilms (A-B) Iridescent floating iron films at the WAI and sampled using a glass slide. (C) Cross-section of the film. (D) Rod-like microbial colonies embedded in brown iron film from JS_DSH lake sediment. (E-F). "Mushroom-like" microbial aggregates and dense spherical iron nanoparticles on aged brown iron films. (G) Brightfield fluorescence microscopy image of aged iron films, showing crystalline-organic structures. (H) XPS analysis of iron biofilm revealing elemental composition and oxidation states, including mixed iron(II/III), copper, and sulfur species.

However, microbial morphologies and densities varied (Figure S6). Nanoparticles were observed attached to microbial surfaces, and mucilaginous structures often interwove with or were embedded in the mineral matrix (Figures 5F & S7). This gelatinous biofilm structure may have enhanced the resistance of gas exchange at the WAI, acting as a methane-barrier.[44]

Chemical roles of iron biofilms

The iron-rich films (42% Fe by mass) not only serve as physical barriers but also form a dynamic redox-active platform that may chemically regulate methane oxidation. Both copper- and iron-dependent methane monooxygenases are capable of directly oxidizing methane.[45] XPS analysis revealed mixed iron(II/III), copper, and sulfur species (Figure 5H), indicative of active redox cycling at the WAI. XRD analysis revealed that fresh films primarily contain amorphous iron (hydr)oxides, whereas aged films develop crystallized minerals (e.g., magnetite and hematite; Figures S7 & 5G). Fluorescence microscopy further confirmed the coexistence of crystalline minerals and organic particulates (Figures 5G & S8), supporting the role of aged biofilms as mineral-organic composites with potential catalytic and microbial functions for methane transformation.

Explanation for methane emission paradox

The methane-barrier effect of floating iron biofilms helps explain the controversial relationship between straw incorporation rates (0–12 t ha^{-1}) and methane emissions (Figures 6A–B). Consistent with previous studies,[27] a higher straw amendment did not necessarily increase methane emissions. Our findings suggest that the formation and activity of iron biofilms critically modulate this relationship.

We observed a strong inverse correlation between iron film biomass (g m^{-2}) and methane flux normalized by OM content (R^2 = 0.96, p < 0.001; Figure 6C). This indicates that increased iron biofilm development effectively suppresses methane emissions, even under high OM inputs from straw amendments.

Moreover, both floating iron biofilms and suspended iron flocs were enriched with methane-oxidizing *pmoA* genes (Figure 3D). This genetic evidence supports the hypothesis that iron biofilms facilitate methane oxidation and thereby reduce net emissions.

DISCUSSION

Landscape-scale scenarios of iron film formation and impact

The diffusion of ferrous ions into overlying waters, followed by oxidation and precipitation, is a ubiquitous process across aquatic environments. Typically, the redistribution of iron across the SWI-WAI could only be inferred by chemical analysis.[29] However, in iron-rich environment under flooded conditions, especially in shallow water systems, landscape-scale iron redistribution can become visually apparent through the formation of iron film

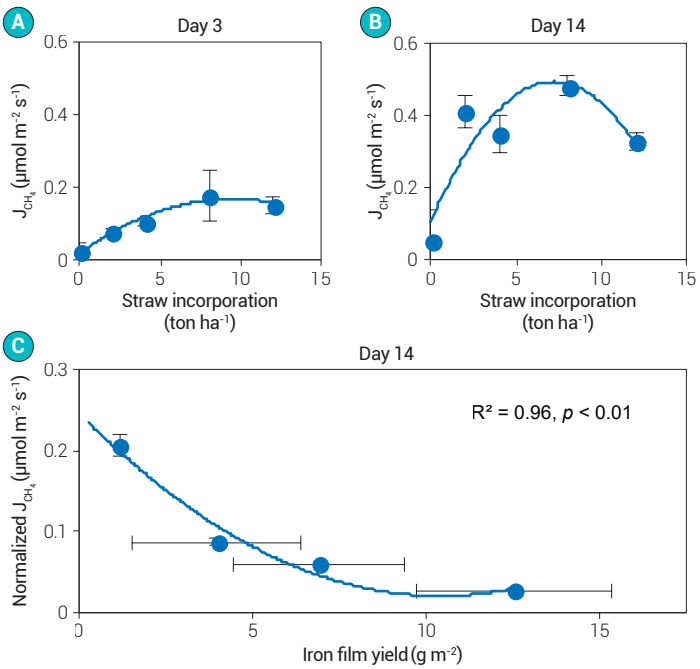

Figure 6. Methane flux dynamics and their relationship with straw addition and floating iron biofilm formation after rice harvest from JS_YCH soils (A-B) Methane flux measured on Day 3 (during initial iron-rich film formation) and Day 14 (post-straw incorporation) under varying straw return rates (0–12 ha^{-1}). (C) Methane flux on Day 14 normalized by the mass of incorporated straw.

(Figure 7). These scenarios highlight the potential role of iron biofilms in regulating methane emissions.

In agricultural systems,[29] nutrient-rich environments like rice paddies, ponds, and lakes receive excessive OM inputs from fertilizers and crop residues, making them hotspots for methane emissions. Yet, the potential contribution of iron biofilms to methane mitigation remains underexplored. In swamps and permafrost regions,[46,47]—naturally enriched with iron and OM—redox fluctuations driven by water table shifts and thawing processes introduce uncertainties in methane budgets; here, iron films may play a critical but underappreciated role in stabilizing these dynamics.

In other systems such as iron-rich groundwater upwelling, irrigation networks, or acid mine drainage sites,[35,48] large-scale reddish iron precipitates often form at the surface even in the absence of abundant OM. While these environments are not typically linked to high methane emissions, their iron-rich biofilms could still influence methane dynamics.

Iron minerals are critical surfaces for biofilm formation and methane oxidation in stratified water systems.[5,15,18,28,49,50] However, their importance in shallow wetlands like rice paddies, ditches and ponds remains understudied.[12,14,51] In these environments, the redistribution of iron from sediment or soil into the SWI and WAI is significant.[29] Given that rice paddies emit ~11% of global anthropogenic methane emissions, a better understanding iron biofilm dynamics is crucial. However, quantifying the contributions of iron biofilms on methane oxidations remains challenging due to a lack of dedicated studies, underscoring the need for further investigation into their global methane budget impacts.

Unique structure and overlooked function of iron biofilms

Up to 80% of prokaryotes in nature are estimated to live as biofilms on mineral surfaces.[52] The methane-barrier function described here enhances our understanding of the role of mineral–microbe interactions at the WAI. Initially studied in acid mine drainage, these films were considered products of iron-oxidizing bacteria and sinks for heavy metals.[35] More recently, such films and flocs have been identified in circumneutral wetlands as dynamic hotspots for iron cycling that may influence carbon dynamics.[31,41,46] Such redox-active films, composed of mixed-valence of iron and copper could theoretically mediate methane oxidation by acting as electron acceptors or catalysts (e.g., via Fenton-like reactions generating hydroxyl radicals[53] or mineral-mediated electron transfer[28,45]). Even in the absence of iron minerals, neuston bacteria[32] thrive at the WAI, forming biofilms and reducing gas exchange.[38,44,54] The floating iron biofilm described in this study is a previously unreported composite structure—neither solely mineral or microbial. It exhibits a pronounced methane-trapping and oxidative functions under circumneutral wetland conditions (mean pH = 6.5, n = 30, Table S1). We speculate that the mineral and microbial layers interact symbiotically: minerals provide a scaffold for functionally relevant microbes, while microbes secrete extracellular polymeric substances that stabilize the mineral matrix.

Methodology advances novel film concept

Conventional studies of microbial biofilm in the bulk sediments and soils typically focus on microaggregates composed of mixed mineral and organic particles, which remain highly heterogeneous. In contrast, our methodological approach physically decouples iron film formation from microbial colonization, allowing the latter to occur during the later stages of iron aging (i.e., "iron film first, microbial colonization later", Figures 5 & 7F; see also Discussion S1). This strategy enabled us to selectively capture microbial communities that are actively functioning at the WAI, rather than passive background populations (Figure 4). Supporting this view, microbial co-occurrence analysis showed a minimal overlap in genus-level taxa between iron biofilms and their underlying sediments and soils. This approach effectively filters out background microbial "noise", enhancing the resolution of functionally relevant communities that directly interact with the biofilm interface.

Implications for nature-based solutions

Floating iron biofilms offer promising potential as a nature-based solution for mitigating methane emissions. The effectiveness of iron amendments in reducing methane emission is well documented, particularly in paddy soils.[55] Our findings show that Iron biofilms form rapidly under controlled conditions, especially with fresh OM inputs, and maintain stable nanostructures even after drying. Even when the films decay from water surface, they settle onto sediment or soil surface (Figure S9 and refs[16,46]), functioning similarly to iron oxide amendments for methane mitigation in freshwater wetlands.[55,56]

Future directions

The methane-barrier effect, along with high *pmoA* gene abundances suggests that substantial methane oxidation occurs at the WAI—a process influenced by both microbial activity and the gas residence time in the water column. Although previous studies have demonstrated a significant methane oxidation at the WAI revealed by isotopic method,[38] we did not provide such evidence, which may show potential limitations in data interpretation.

Additionally, while iron-driven chemical pathways may synergize with microbial methane oxidation,[45] they were not explicitly investigated in this study. Our work emphasizes the microbial contribution to methane suppression, but abiotic iron-OM interactions remain an important future research avenue.

Although measured methane flux were about 2 times lower than predicted, current work does not allow to make global-scale estimations of how much methane oxidation was mitigated by iron biogeochemistry but shows a great potential for broader-scale evaluations.

Finally, the discovery of floating iron biofilms opens a new frontier in iron–carbon interactions at the WAI. The microbial colonization and development, including those of bacteria and viruses, within these biofilms may represent a model system for studying ecological adaption and microbial evolution under redox-dynamic, interface-specific conditions. Future metagenomic approaches could yield novel insights into these complex interactions.[42,57,58]

CONCLUSION

This study identifies floating iron biofilms at the WAI as a critical and previously overlooked methane-barrier in wetlands. These biofilms form rapidly under high OM conditions, creating a dual-layer structure that combines physical trapping by iron minerals and microbial oxidation via methanotrophs. This mechanism suppresses methane emissions significantly, explaining emission paradoxes in environments like straw-amended rice paddies. The biofilms' durability, rapid formation, and function under controlled conditions highlight their viability as scalable, nature-based solu-

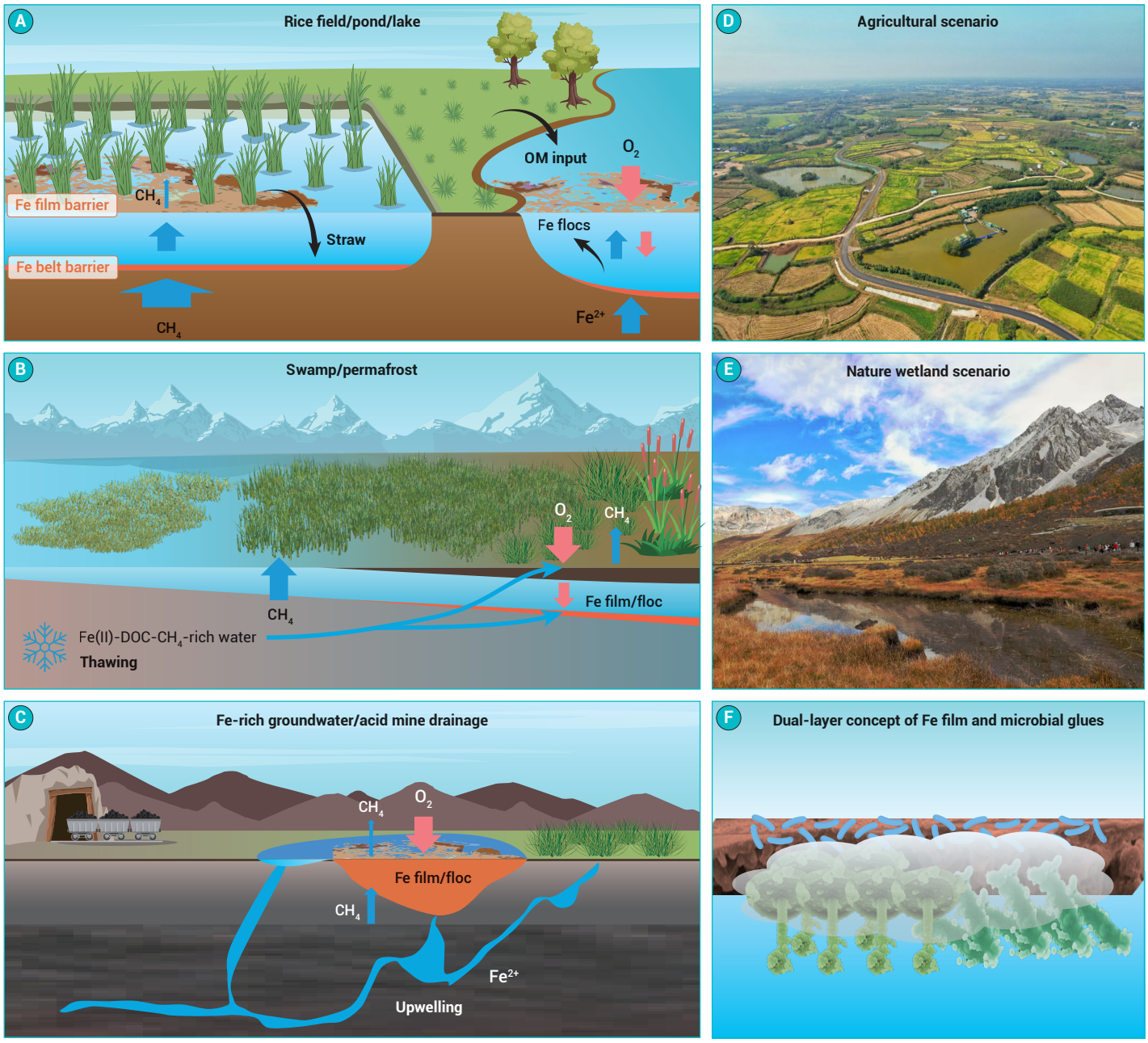

Figure 7. Typical scenarios of iron film formation and structures in the environment (A, D) Agricultural scenarios: Rice fields, ponds, drainage ditches, and lakes are often nutrient-rich due to fertilizer application and straw residues, promoting iron film formation. (B, E) Natural wetland scenarios: Swamps and permafrost regions are naturally enriched with iron and OM. Redox fluctuations driven by water table changes and thawing processes can lead to high uncertainty in methane emissions. (C) Iron-rich groundwater upwelling and acid mine drainage: Iron films can form extensively in surface waters, even under low-OM conditions. (F) Conceptual diagram of the dual-layer structure of iron biofilms, highlighting mineral and microbial interactions. Photos D and E were taken in Hefei, Anhui and on the Tibet Plateau, China.

tions for mitigating agricultural methane emissions. By shifting attention from traditional SWI processes to those occurring at the WAI, this work reshape current paradigms of wetland methane regulation and highlight the broader role of iron biogeochemistry in the global methane budget.

REFERENCES

1. Forbrich I., Yazbeck T., Sulman B., et al. (2024). Three decades of wetland methane surface flux modeling by earth system models-advances, applications, and challenges. *J. Geophys. Res. Biogeosci.* **129**:e2023JG007915. DOI:10.1029/2023JG007915
2. Saunois M., Martinez A., Poulter B., et al. (2024). Global Methane Budget 2000–2020. *Earth Syst. Sci. Data Discuss.* **2024**:1–147. DOI:10.5194/essd-2024-115
3. Rosentreter J. A., Alcott L., Maavara T., et al. (2024). Revisiting the global methane cycle through expert opinion. *Earth Future* **12**:e2023EF004234. DOI:10.1029/2023EF004234
4. Koffi E. N., Bergamaschi P., Alkama R., et al. (2020). An observation-constrained assessment of the climate sensitivity and future trajectories of wetland methane emissions. *Sci. Adv.* **6**:eaay4444. DOI:10.1126/sciadv.aay4444
5. Cabrol L., Thalasso F., Gandois L., et al. (2020). Anaerobic oxidation of methane and associated microbiome in anoxic water of Northwestern Siberian lakes. *Sci. Total Environ.* **736**:139588. DOI:10.1016/j.scitotenv.2020.139588
6. Rocher-Ros G., Stanley E. H., Loken L. C., et al. (2023). Global methane emissions from rivers and streams. *Nature* **621**:530–535. DOI:10.1038/s41586-023-06344-6
7. Rosentreter J. A., Borges A. V., Deemer B. R., et al. (2021). Half of global methane emissions come from highly variable aquatic ecosystem sources. *Nat. Geosci.* **14**:225–230. DOI:10.1038/s41561-021-00715-2
8. Mao S.H., Wang J.Y., Joye S., et al. (2024). Marine methane paradox: Enigmatic production of methane in oxygenated waters. *Innov. Geosci.* **2**:100071. DOI:10.59717/j.xinn-geo.2024.100071
9. Zhang H., Wei T., Zhang J., et al. (2024). Microbial mediation of cryptic methane cycle in semiclosed marine water column. *Innov. Geosci.* **2**:100082. DOI:10.59717/j.xinn-

geo.2024.100082
10. Wang S., Sun P., Zhang G., et al. (2022). Contribution of periphytic biofilm of paddy soils to carbon dioxide fixation and methane emissions. *Innov.* **3**. DOI:10.1016/j.xinn.2021.100192.
11. Le Mer J. and Roger P. (2001). Production, oxidation, emission and consumption of methane by soils: a review. *Eur. J. Soil Biol.* **37**:25–50. DOI:10.1016/S1164-5563(01)01067-6
12. Perryman C. R., Bowen J. C., Shahan J., et al. (2024). Fate of methane in canals draining tropical peatlands. *Nat. Commun.* **15**:9766. DOI:10.1038/s41467-024-54063-x
13. Yanagawa K., Okabeppu M., Kikuchi S., et al. (2025). Vertical distribution of methanotrophic archaea in an iron-rich groundwater discharge zone. *PLoS One* **20**:e0319069. DOI:10.1371/journal.pone.0319069
14. Yang W. H., McNicol G., Teh Y. A., et al. (2017). Evaluating the classical versus an emerging conceptual model of peatland methane dynamics. *Global Biogeochem. Cycles* **31**:1435–1453. DOI:10.1002/2017GB005622
15. Lapham L. L., Lloyd K. G., Fossing H., et al. (2024). Methane leakage through the sulfate–methane transition zone of the Baltic seabed. *Nat. Geosci.* **17**:1277–1283. DOI:10.1038/s41561-024-01594-z
16. Riedinger N., Formolo M. J., Lyons T. W., et al. (2014). An inorganic geochemical argument for coupled anaerobic oxidation of methane and iron reduction in marine sediments. *Geobiology* **12**:172–181. DOI:10.1111/gbi.12077
17. Bar-Or I., Elvert M., Eckert W., et al. (2017). Iron-coupled anaerobic oxidation of methane performed by a mixed bacterial-archaeal community based on poorly reactive minerals. *Environ. Sci. Technol.* **51**:12293–12301. DOI:10.1021/acs.est.7b03126
18. Lopes F., Viollier E., Thiam A., et al. (2011). Biogeochemical modelling of anaerobic vs. *aerobic methane oxidation in a meromictic crater lake (Lake Pavin, France). Appl. Geochem.* **26**:1919–1932. DOI:10.1016/j.apgeochem.2011.06.021
19. Żygadłowska O. M., Venetz J., Lenstra W. K., et al. (2024). Ebullition drives high methane emissions from a eutrophic coastal basin. *Geochim. Cosmochim. Acta* **384**:1–13. DOI:10.1016/j.gca.2024.08.028
20. Egger M., Riedinger N., Mogollón J. M., et al. (2018). Global diffusive fluxes of methane in marine sediments. *Nat. Geosci.* **11**:421–425. DOI:10.1038/s41561-018-0122-8
21. Beaulieu J. J., DelSontro T. and Downing J. A. (2019). Eutrophication will increase methane emissions from lakes and impoundments during the 21st century. *Nat. Commun.* **10**:1375. DOI:10.1038/s41467-019-09100-5
22. Egger M., Rasigraf O., Sapart C. J., et al. (2015). Iron-mediated anaerobic oxidation of methane in brackish coastal sediments. *Environ. Sci. Technol.* **49**:277–283. DOI:10.1021/es503663z
23. Jiang Y., Qian H., Huang S., et al. (2019). Acclimation of methane emissions from rice paddy fields to straw addition. *Sci. Adv.* **5**:eaau9038. DOI:10.1126/sciadv.aau9038
24. Borges A. V., Deirmendjian L., Bouillon S., et al. (2022). Greenhouse gas emissions from African lakes are no longer a blind spot. *Sci. Adv.* **8**:eabi8716. DOI:10.1126/sciadv.abi8716
25. Wen Z., Song K., Zhao Y., et al. (2016). Carbon dioxide and methane supersaturation in lakes of semi-humid/semi-arid region, Northeastern China. *Atmos. Environ.* **138**:65–73. DOI:10.1016/j.atmosenv.2016.05.009
26. Zhou L., Zhou Y., Zhang Y., et al. (2025). Rainstorm-induced organic matter pulses: A key driver of carbon emissions from inland waters. *Innov.* **6**. DOI:10.1016/j.xinn.2024.100746.
27. Nikolaisen M., Cornulier T., Hillier J., et al. (2023). Methane emissions from rice paddies globally: A quantitative statistical review of controlling variables and modelling of emission factors. *J. Clean. Prod.* **409**:137245. DOI:10.1016/j.jclepro.2023.137245
28. Kappler A., Bryce C., Mansor M., et al. (2021). An evolving view on biogeochemical cycling of iron. *Nat. Rev. Microbiol.* **19**:360–374. DOI:10.1038/s41579-020-00502-7
29. Ratering S. and Schnell S. (2000). Localization of iron-reducing activity in paddy soilby profile studies. *Biogeochemistry* **48**:341–365. DOI:10.1023/A:1006252315427
30. Zhang H., Rush Z., Penn Z., et al. (2024). Films floating on water surface: Coupled redox cycling of iron species (Fe (III)/Fe (II)) at soil/water and water/air interfaces. *Water* **16**:1298. DOI:10.3390/w16091298
31. Dong L., Chen M., Liu C., et al. (2024). Microbe interactions drive the formation of floating iron films in circumneutral wetlands. *Sci. Total Environ.* **906**:167711. DOI:10.1016/j.scitotenv.2023.167711
32. Cunliffe M., Engel A., Frka S., et al. (2013). Sea surface microlayers: A unified physicochemical and biological perspective of the air–ocean interface. *Prog. Oceanogr.* **109**:104–116. DOI:10.1016/j.pocean.2012.08.004
33. Davison W. (1993). Iron and manganese in lakes. *Earth-Sci. Rev.* **34**:119–163. DOI:10.1016/0012-8252(93)90029-7
34. Kleja D. B., van Schaik J. W. J., Persson I., et al. (2012). Characterization of iron in floating surface films of some natural waters using EXAFS. *Chem. Geol.* **326–327**:19-26. DOI:10.1016/j.chemgeo.2012.06.012.
35. Sánchez-España J., Ilin A. M., Yusta I., et al. (2023). Fe (III) biomineralization in the surface microlayer of acid mine waters catalyzed by neustonic Fe (II)-oxidizing microorganisms. *Minerals* **13**:508. DOI:10.3390/min13040508
36. Grathoff G. H., Baham J. E., Easterly H. R., et al. (2007). Mixed-valent Fe films ('schwimmeisen') on the surface of reduced ephemeral pools. *Clays Clay Miner.* **55**:635–643. DOI:10.1346/CCMN.2007.0550610
37. Ueyama M., Takeuchi R., Takahashi Y., et al. (2015). Methane uptake in a temperate forest soil using continuous closed-chamber measurements. *Agric. For. Meteorol.* **213**:1–9. DOI:10.1016/j.agrformet.2015.05.004
38. Happell J. D., Chanton J. P. and Showers W. J. (1995). Methane transfer across the water - air interface in stagnant wooded swamps of Florida: Evaluation of mass - transfer coefficients and isotropic fractionation. *Limnol. Oceanogr.* **40**:290–298. DOI:10.4319/lo.1995.40.2.0290
39. Goldman J. C., Dennett M. R. and Frew N. M. (1988). Surfactant effects on air-sea gas exchange under turbulent conditions. *Deep Sea Research Part A. Oceanographic Research Papers* **35**:1953–1970. DOI:10.1016/0198-0149(88)90119-7
40. Mustaffa N. I. H., Ribas-Ribas M., Banko-Kubis H. M., et al. (2020). Global reduction of *in situ* CO_2 transfer velocity by natural surfactants in the sea-surface microlayer. *Proc. R. Soc. A: Math. Phys. Eng. Sci.* **476**:20190763. DOI. DOI:10.1098/rspa.2019.0763
41. Drudge C. N. and Warren L. A. (2014). Diurnal floc generation from neuston biofilms in two contrasting freshwater lakes. *Environ. Sci. Technol.* **48**:10107–10115. DOI:10.1021/es503013w
42. Wang Y.-F., Xu J.-Y., Liu Z.-L., et al. (2024). Biological interactionsmediate soil functions by altering rare microbial communities. *Environ. Sci. Technol.* **58**:5866–5877. DOI:10.1021/acs.est.4c00375
43. Perkins R. B., Gray Z. N., Grathoff G., et al. (2016). Characterization of natural and synthetic floating iron surface films and their associated waters. *Chem. Geol.* **444**:16–26. DOI:10.1016/j.chemgeo.2016.09.027
44. Pereira R., Ashton I., Sabbaghzadeh B., et al. (2018). Reduced air–sea CO_2 exchange in the Atlantic Ocean due to biological surfactants. *Nat. Geosci.* **11**:492–496. DOI:10.1038/s41561-018-0136-2
45. Tucci F. J. and Rosenzweig A. C. (2024). Direct methane oxidation by copper- and iron-dependent methane monooxygenases. *Chem. Rev.* **124**:1288–1320. DOI:10.1021/acs.chemrev.3c00727
46. ThomasArrigo L. K., Notini L., Shuster J., et al. (2022). Mineral characterization and composition of Fe-rich flocs from wetlands of Iceland: Implications for Fe, C and trace element export. *Sci. Total Environ.* **816**:151567. DOI:10.1016/j.scitotenv.2021.151567
47. Chauhan A., Patzner M. S., Bhattacharyya A., et al. (2024). Interactions between iron and carbon in permafrost thaw ponds. *Sci. Total Environ.* **946**:174321. DOI:10.1016/j.scitotenv.2024.174321
48. Garnier J., Garnier J. M., Vieira C. L., et al. (2017). Iron isotope fingerprints of redox and biogeochemical cycling in the soil-water-rice plant system of a paddy field. *Sci. Total Environ.* **574**:1622–1632. DOI:10.1016/j.scitotenv.2016.08.202
49. Reis P. C. J., Tsuji J. M., Weiblen C., et al. (2024). Enigmatic persistence of aerobic methanotrophs in oxygen-limiting freshwater habitats. *ISME J.* **18**. DOI:10.1093/ismejo/wrae041.
50. Oswald K., Milucka J., Brand A., et al. (2016). Aerobic gammaproteobacterial methanotrophs mitigate methane emissions from oxic and anoxic lake waters. *Limnol. Oceanogr.* **61**:S101–S118. DOI:10.1002/lno.10312
51. Gan D., Zhang Z., Li H., et al. (2024). Ditch emissions partially offset global reductions in methane emissions from peatland drainage. *Commun. Earth Environ.* **5**:640. DOI:10.1038/s43247-024-01818-5
52. Penesyan A., Paulsen I. T., Kjelleberg S., et al. (2021). Three faces of biofilms: a microbial lifestyle, a nascent multicellular organism, and an incubator for diversity. *NPJ Biofilms Microbiome* **7**:80. DOI:10.1038/s41522-021-00251-2
53. Liu J., Zhu C., Zhu F., et al. (2024). Strong substance exchange at paddy soil-water interface promotes nonphotochemical formation of reactive oxygen species in overlying water. *Environ. Sci. Technol.* **58**:7403–7414. DOI:10.1021/acs.est.3c10866
54. Cunliffe M., Upstill-Goddard R. C. and Murrell J. C. (2011). Microbiology of aquatic surface microlayers. *FEMS Microbiol. Rev.* **35**:233–246. DOI:10.1111/j.1574-6976.2010.00246.x
55. Huang B., Yu K. and Gambrell R. P. (2009). Effects of ferric iron reduction and regeneration on nitrous oxide and methane emissions in a rice soil. *Chemosphere* **74**:481–486. DOI:10.1016/j.chemosphere.2008.10.015
56. Yu Y., Feng Y., Yu Y., et al. (2024). Closing the gap between climate regulation and food security with nano iron oxides. *Nat. Sustain.* **7**:758–765. DOI:10.1038/s41893-024-01334-6
57. Wang L., Lin D., Xiao K.-Q., et al. (2024). Soil viral–host interactions regulate microplastic-dependent carbon storage. *Proc. Natl. Acad. Sci.* **121**:e2413245121. DOI:10.1073/pnas.2413245121
58. Zhu D., Liu S.-Y., Sun M.-M., et al. (2024). Adaptive expression of phage auxiliary metabolic genes in paddy soils and their contribution toward global carbon sequestration. *Proc. Natl. Acad. Sci.* **121**:e2419798121. DOI:10.1073/pnas.2419798121

FUNDING AND ACKNOWLEDGMENTS

This work was financially supported by the National Natural Science Foundation of China (Grant No. 42477116) for laboratory expenditures. The authors thank Ms. Xiao Zhou for her expert technical assistance throughout this project. The first author specifically acknowledges Dr. Dong Zhu for stipend support during manuscript preparation. The funders had no role in study design, data collection and analysis, decision to publish, or preparation of the manuscript.

AUTHOR CONTRIBUTIONS

S.Z. conducted this research independently, managing the study, including experimental design, data collection, and manuscript preparation, under the supervision of Z.C., who provided critical guidance and support for experimental resources. H.F.Q.R performed the microscope analysis. D.Z. contributed data analysis and discussions. All authors contributed to the manuscript and approved the final version.

DECLARATION OF INTERESTS

The authors declare no competing interests.

DATA AND CODE AVAILABILITY

All data is available in the manuscript and supplementary information. Raw 16S rRNA sequences are accessible at https://www.ncbi.nlm.nih.gov/sra/PRJNA1216303. Source data are provided with this paper. All code and source data necessary for replicating reported results are available in the https://github.com/xjtluhes/floating-iron-biofilms at manuscript submission.

SUPPLEMENTAL INFORMATION

It can be found online at https://doi.org/10.59717/j.xinn-geo.2025.100161

LEAD CONTACT WEBSITE

Zheng Chen: https://scholar.xjtlu.edu.cn/en/persons/ZhengChen